

Article

Oscillating Heat Pipe Cooling System of Electric Vehicle's Li-Ion Batteries with Direct Contact Bottom Cooling Mode

Ri-Guang Chi and Seok-Ho Rhi *

Applied Thermal Engineering Lab, School of Mechanical Engineering, Chungbuk National University, 1 ChungDae-ro, SeoWon-gu, Cheongju, Chungbuk 28644, Korea; jiyirguang@naver.com

* Correspondence: rhi@chungbuk.ac.kr

Received: 30 March 2019; Accepted: 30 April 2019; Published: 5 May 2019



Abstract: Recently, the use of electrical vehicles has abruptly increased due to environmental crises. The high energy density of lithium-ion batteries is their main advantage for use in electric vehicles (EVs). However, the thermal management of Li-ion batteries is a challenge due to the poor heat resistance of Lithium ions. The performance and lifetime of lithium ion batteries are strongly affected by the internal operating temperature. Thermal characterization of battery cells is very important to ensure the consistent operation of a Li-ion battery for its application. In the present study, the OHP (Oscillating Heat Pipe) system is proposed as a battery cooling module, and experimental verification was carried out. OHP is characterized by a long evaporator section, an extremely short condenser section, and almost no adiabatic section. Experimental investigations were conducted using various parameters such as the filling ratio, orientation, coolant temperature, and heat flux. Average temperature of the heater's surface was maintained at 56.4 °C using 14 W with 25 °C coolant water. The experimental results show that the present cooling technology basically meets the design goal of consistent operation.

Keywords: Oscillating Heat Pipe; Li-ion battery cooling; electric vehicles; heat transfer; battery thermal management

1. Introduction

Climate and environmental crisis problems that have emerged in recent years, have led to the proposition of new energy solutions, including the substitution of combustion engines by electrical systems accompanied with Li-ion batteries. The CO₂ intensity of electric vehicles (EVs) can be determined by the specific mixture of power generation sources used for driving, such as coal, nuclear, or renewable power sources, as well as the carbon intensity of the vehicle manufacturing process. The high energy efficiency components of electric vehicles allow them to significantly cut CO₂ emissions with respect to internal combustion engines. The IEA (International Energy Agency) (2017a) observed that, in 2015, electric cars in Europe emitted ~50% less CO₂ than gasoline cars and 40% less than diesel cars [1].

To increase the driving range of EVs, a large number of high energy density Lithium-ion batteries should be installed. However, Lithium-ion batteries have a shortcoming in heat resistance—a temperature that is too high or too low will result in a drastic reduction in battery capacity and service life [2,3]. Studies have shown that the heat inside Lithium-ion batteries is mainly induced from reactions that produce Ohmic heat and polarization heat [4–6]. Various models have been proposed based on these heat generation mechanisms. Among them, the most widely used model is the Bernardi model because of its simple logics and reasonable accuracy [7]. Heubner et al. [8] conducted research

on the heat generation of a LiCO₂/graphite lithium ion battery with a 0.2–1 C discharge rate (discharge rate 1 C = battery capacity/one hour). Total heat generation was between 50 and 150 kJ/L. Liu [9] carried out the research on cell aging due to heat generation under conditions of 2 and 4 C. The maximum heat generation was 9 and 35 W, respectively. Todd M. Bandhauer [10] investigated the heat generation of C/LiFePO₄ lithium ion batteries with different current magnitudes. He reported that heat generation reached 200 W/L with a current of 5 A. Heat generation from a LiFePO₄ (20 Ah) battery was investigated by Panchal [11], who showed that the rate of heat generation was 13 W for a discharge rate of 1 C.

Conventional air cooling and water cooling methods have been used to solve the thermal problem of batteries. Choi [12] investigated the effect of the wind speed on air cooling using a battery size of 240 mm × 130 mm × 13.4 mm, a channel size of 210 mm × 2–6 mm, and a coolant flow rate of 2–6 m³/h. Under a wind speed of 6 m³/h and a 40 A square pulse cycle, the temperature of the battery cell was maintained at about 37.5 °C. Yu [13] conducted air convection cooling for a battery pack with a size of 620 mm × 430 mm × 310 mm and a coolant flow rate of 0.1–2 m³/min. Under a 1 C discharge rate and an air flow rate of 2 m³/min, the maximum temperature of the new battery pack was reduced by nearly 4.5 °C compared to the original pack. Ling [14] performed research work on air cooling methods for 18,650 battery cooling. The spacing between centers of two neighboring cells was 30 mm and the wind speed was varied between 1 and 5 m/s. Under a discharge rate of 1.5 C and an air speed of 1 m/s, the battery's maximum temperature rose sharply to 60 °C, and under air speeds higher than 3 m/s, the temperature was kept below 45 °C. Bai [15] reported a PCM (phase change material) battery cooling method with a water flowing cold plate. The battery size used was 170 mm × 230 mm × 12 mm, the height of the cold plate was 2–7 mm, and the mass flow rate was 0.25–3 g/s. After five continuous charge–discharge cycles at 0.5 and 2 C, the maximum temperature was kept below 42 °C. However, due to the small flow passage, a 42 Pa pressure drop was observed at a channel width of 3 mm. Tong [16] investigated various parameters of a cooling system with a water coolant plate, such as the flow rate, section size, and discharge rate. Under a coolant velocity of 0.1 m/s and a discharge rate of 1 C, the average temperature difference was only 2 °C. Huo [17] investigated a mini channel cold plate cooling system with six 1 mm thick micro channels. At a flow rate of 1 kg/s, the maximum temperature was maintained between 30 and 32 °C. However, the pressure loss reached 478 Pa. To make the data compatible for EV/HEV (hybrid electric vehicle) application, Panchal [18] developed a modified exponential–polynomial equivalent circuit model to simulate the temperature and voltage fields with water cooling. Under a discharge rate of 1–2 C and working temperatures of 5, 15, 25, and 35 °C, the model showed good agreement with the experimental results.

However, due to the low thermal conductivity of air and the large volume of the air cooling system, the cooling system requires a large heat transfer surface area and flow passage for air convection cooling. Furthermore, due to the high viscosity of water, the water cooling system requires extra energy to circulate liquid.

The importance of the heat pipe as a thermal superconductor for thermal management is gradually being realized. Liu [19] carried out research on battery cooling with an ultra-thin micro heat pipe (168 mm × 10 mm × 1 mm). In their system, one end of the heat pipe is inserted between the batteries, and the other end is a finned sink. When air cooling was conducted at a discharge rate of 3 C, the maximum temperature of the battery was 53 °C. Wang [20] investigated the battery cooling method with an L-shaped heat pipe. The heat pipe evaporation section was flattened (120 mm × 13.16 mm × 4.5 mm), and the lower condensation section was cylindrical (length = 50 mm and diameter = 10 mm). Under a heating rate of 20 W/cell, the maximum temperature of the battery was about 50 °C. Hong [21] investigated the loop heat pipe battery cooling system with system inclination and battery heat generation. The evaporation section of a loop heat pipe is a flat plate with 25 micro-channels (width = 3 mm and depth = 0.6 mm) inside it. The inner and outer diameters of the loop pipe were 2.4 and 3 mm, respectively.

Due to the importance of thermal management in high heat generation Li-ion batteries, heat pipes are adopted in many cooling system as an efficient heat transfer device, but most heat pipe-adapted cooling systems are bottom heating-top or side cooling systems. These types of cooling system have good cooling performance but take up a lot of space. In addition, their structures are not convenient in terms of battery maintenance.

OHP, a highly efficient and simple-structured type of heat pipe, is now being studied extensively. As shown in Figure 1, it consists of a curved channel and working fluid, which can be described as the evaporator, adiabatic, and condenser sections. Because the vapor bubble is separated by multiple liquid slugs, when the heat is supplied to the evaporator section, a pressure difference is created between the bubbles, causing the liquid plug to oscillate between the evaporator section and the condenser section, thereby transferring heat.

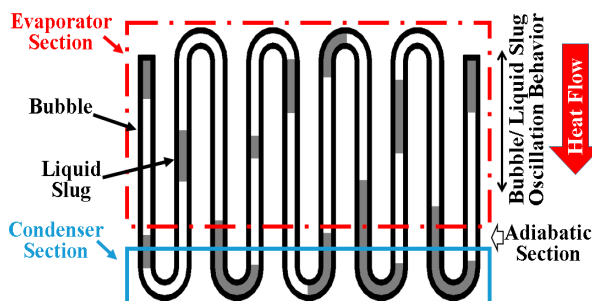


Figure 1. Oscillating heat pipe as a bottom cooling mode.

Rao [22] studied the OHP (four turns, inner diameter = 1.8 mm, and outer diameter = 3 mm) for battery cooling. Under 20 W of heating, at 800 s, steady state was reached, and the maximum temperature was about 55 °C. In another paper, Rao reported on a cooling system that combined OHP and PCM (phase change material) [23]. Although its cooling performance was shown to be good, it is still bottom heating/top cooling. Qu [24] used a special OHP for the battery thermal management of hybrid-electric vehicles. The condensation section and evaporation section of OHP were a micro-grooved copper tube system. At 121 W, the micro-grooved cooling system could maintain a temperature of 50 °C.

Chi [25] proposed a top heating/bottom cooling OHP model shown in Figure 1. As shown in Figure 2a, their OHP cooling system has the conventional rounded lower end with a short (15 mm) condenser section. However, as the number of OHP increases, the structure of cooling of system will also become more complicated.

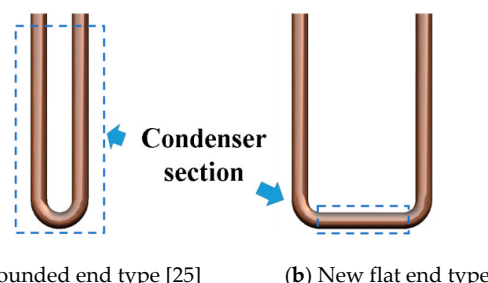


Figure 2. Configuration of the OHP condenser section.

According to the cooling method used to transfer heat from the battery to the outside environment, cooling technology can carry out various liquid cooling methods (air, water, oil-based fluids, and refrigerants, etc.) and PCM. In addition, heat pipe cooling technology is also under development [7,26].

Table 1 shows the comparison of various cooling methods. As described in Table 1, liquid cooling methods are mainly divided into direct and indirect method. The direct cooling type involves direct immersion of the battery into the high-resistance coolant, so the cooling efficiency is very high. However, there are several problems, such as electrical short-circuiting, electrochemical corrosion, and sealing. Furthermore, the battery is immersed in the coolant, so maintenance and replacement will be very troublesome. Indirect type involves letting water flow through the channel between the batteries. Compared with the direct type, some problems are alleviated, but since the channels are generally small and the pressure drop is also very large, the pump consumes a lot of electric energy, thereby reducing the electric vehicle travel [7,27,28]. Due to the low specific heat and low thermal conductivity, the efficiency of air cooling is very low. However, the structure is simple and there is no disadvantage of water cooling, so the method of increasing the flow rate or the cross-section of the passage is used in the battery cooling of the electric vehicle [7,27,28]. PCM cooling uses the principle of heat absorption during phase change. Although PCM can absorb a large amount of heat, its thermal conductivity is low, for example, paraffin has a thermal conductivity of only 0.149–0.514 W/m·K. The temperature will increase dramatically after PCM melts; therefore, PCM is used in combination with air cooling or liquid cooling. Moreover, the PCM density is large, and if used in a large amount, the battery space is reduced [26,27,29,30].

As a heat superconductor, the heat pipe is capable of rapid heat transfer. In most studies, the cooling section is in the upper part of the battery. This structure affects battery maintenance and updates. As a special heat pipe, OHP can work without gravity. Moreover, it is small in size and diverse in shape, so it can be applied to a large number of diverse batteries. The OHP proposed in this paper has a heating section that is much larger than the cooling section (~20 times), so the cooling effect is not ideal. However, with the adjustment of parameters, we believe that the performance of OHP will get better and better.

Table 1. Comparison of various cooling methods [7,11–30].

	Liquid Cooling [7,15–18,27,28] Direct (Immersion)	Air Cooling [7,12–14,27,28]	PCM [15,23, 26,27,29,30]	Heat Pipe [19–21]	OHP [2–25]
	Indirect				
Cooling efficiency	A	A	B	B	B
System complexity	C	C	A	C	B
System volume	A	A	C	B	A
Energy loss	C	C	A	A	A
Maintenance	C	C	A	B	A
Short circuit	C	C	A	C	A
Lifespan	C	C	A	A	A
Cost	C	C	A	B	B

* A, B, and C mean good, fair, and poor, respectively, in terms of their advantage in a battery cooling system.

The present study investigated an OHP (Oscillating Heat Pipe) battery cooling system with a condenser directly contacting the cold plate surface in bottom cooling mode, as shown in Figure 2. The performance and various effects of the system's operating parameters, such as the charging rate, orientation, pipe size, and supplied heating rate, were assessed.

2. Experiments

Figure 3a–e shows a battery cooling system with the new type of OHP, which will be applied to an electric vehicle. Figure 3b,e shows the present experimental setup accompanied by the OHP. The experimental setup mainly consists of an OHP, a heater, a DC-power supply (DP30-10DU, TOYOTECH, Incheon, Korea), a water flowing cooling plate (0.01 kg/s), and a multichannel data acquisition system (Yokogawa, MX-100). The maximum critical inner diameter of the OHP can be obtained by Equations (1) and (2). Furthermore, the cooling plate has two passing flow channels, as shown in Figure 3c, and is made of aluminum alloy and sealed with a silicone ring. The bottom end outer surface of the condenser section in the OHP directly contacts the top surface of the cooling plate system. In order to reduce the thermal resistance between the cooling plate and the condenser section of the OHP, the condenser end

and the cooling plate were bolt jointed tightly between fixed holding plate-1 and fixed holding plate-2, as shown in Figure 3d.

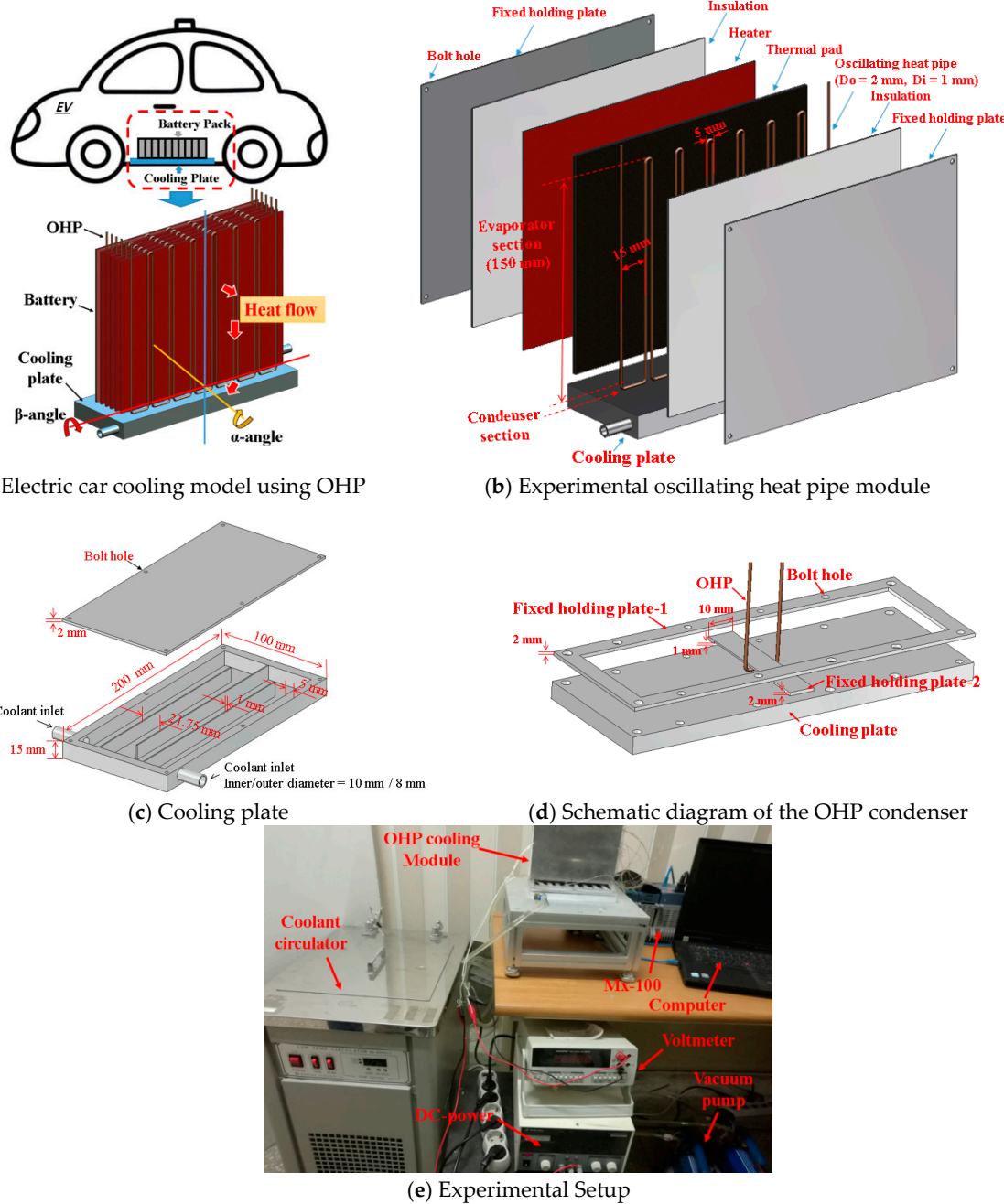


Figure 3. Specific configurations of experimental system.

Despite the simple structure of the OHP, the physical flow behavior inside it is very complex, and its performance is affected by many different parameters, including the thermo physical properties of the working fluid. The OHP channel diameter for randomly separating the pulsating liquid slug/vapor plug flow of the OHP must have a Bond number ≤ 4 , as determined by Equation (1) [31]. If the Bond number is greater than 4, the surface tension will not withstand the buoyancy driven force, and the vapor plug will not be able to collapse, so it will maintain a stable shape.

$$Bo = \frac{g(\rho_l - \rho_v)D_i^2}{\sigma} \quad (1)$$

In light of this, D_{cr} can be defined as Equation (2):

$$D_{cr} = 2 \sqrt{\frac{\sigma}{g(\rho_l - \rho_v)}}. \quad (2)$$

Using Equation (2), when the working fluid is methanol, the critical inner diameter D_{cr} of OHP is ~ 3.2 mm. Based on this critical inner diameter of OHP, a few commercial copper tube combinations were tested. The test OHPs were fabricated using copper capillary tubes ($D_o/D_i = 1.8$ mm/0.8 mm, $D_o/D_i = 2$ mm/1 mm, $D_o/D_i = 2.4$ mm/1.4 mm), and the end side of the evaporator was bent to 180° with a 5 mm curvature diameter. The bottom side of the condenser was a straight pipe of 10 mm length, bent at 90° with a 5 mm curvature diameter. The OHP had eight turns, as shown in Figure 3b. The resistance flat heater (190 mm \times 150 mm) was used to simulate the Li-ion battery, which is modeled as an LG chem Li-ion car battery. Heat generation rates of 10, 14, and 20 Watts were used based on information from the literature [7,11].

In the present experimental system, K-type thermocouples (TT-K-36-SLE, Omega, Stamford, CT, USA) and a data acquisition module (MX-100, Yokogawa, Tokyo, Japan) were used to measure temperatures in many positions. The temperature measurement points of the thermocouples are shown in Figure 4 in the following positions: numbers 1–5 in the heater surface, numbers 6–8 in the upper part of the evaporation section of the OHP, numbers 9–11 in the middle part of the evaporation section of the OHP, numbers 12–14 in the bottom part of the evaporation section of the OHP, numbers 15–17 in the condenser section of the OHP, and numbers 18 and 19 in the coolant outlet and inlet.

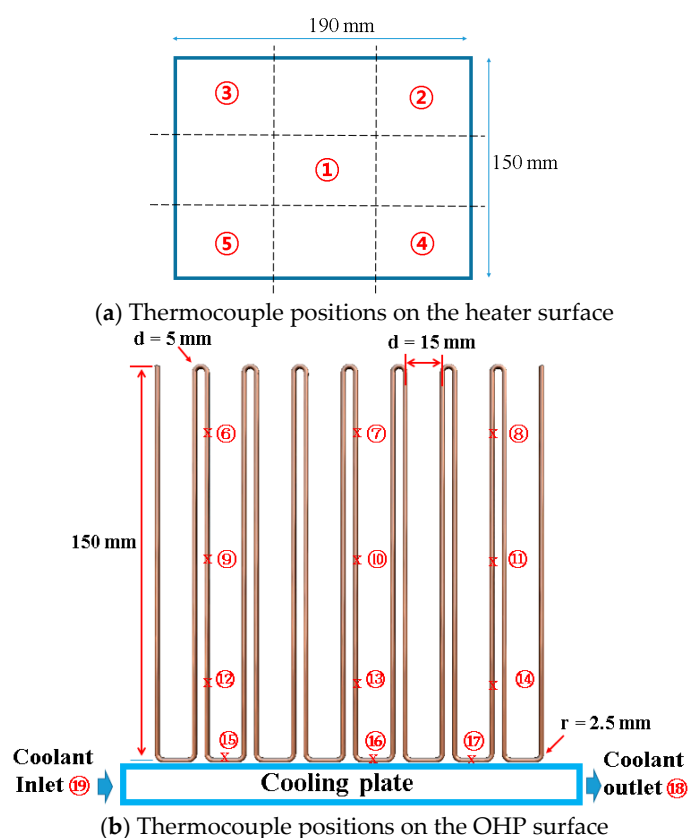


Figure 4. Thermocouple positions.

To estimate the thermal performance of the OHP and the system, the thermal resistances of the OHP and the system were estimated by Equations (3)–(5). The OHP operation based on the charging rate was evaluated with R_{OHP} , where \overline{T}_{evap} , \overline{T}_{cond} , and \overline{T}_{heater} are the average temperatures of the nine evaporator positions, three condenser positions, and five heater positions, respectively, and T_{Cool} is the

coolant inlet point. Input heat was supplied to the evaporator using a DC power transformer through a flat thermal pad. The input power was calculated by Equation (6), where V and I are the input voltage and electric current, respectively [32].

$$\Delta T = \overline{T_{evap}} - \overline{T_{cond}} \quad (3)$$

$$R_{OHP} = \frac{(\Delta T)}{Q} \quad (4)$$

$$R_{SYS} = \frac{(\overline{T_{heater}} - T_{cool})}{Q} \quad (5)$$

$$Q = VI \quad (6)$$

In the present work, the parameters influencing the thermal resistance were the temperature (T), current (I), and voltage (V). The voltage and current error of the DC power supply was $\pm (0.1\% \text{ rdg} + 5 \text{ digits})$, and the temperature error of MX-100 was $\pm (0.05\% \text{ rdg} + 0.7 \text{ }^{\circ}\text{C})$. c_i and σ_i are the sensitivity coefficient and the error of each parameter, respectively, and they were calculated by Equation (7) [33]:

$$c_i = \frac{\partial R_{OHP}}{\partial x_i} \quad (7)$$

Finally, the standard uncertainty error of R_{OHP} , which was calculated by Equation (8), under heating at 10 W was $\pm 0.12 \text{ }^{\circ}\text{C/W}$.

$$\Delta R = \sum_1^i (|c_i \sigma_i|) \quad (8)$$

To analyze the oscillation behavior of the temperature at a specific location on the OHP, the Fast Fourier Transform (FFT) method was applied for temperature position no. 16, which is an interface temperature position between the evaporator and the condenser. The FFT Power Spectrum Density (PSD) was calculated by Equation (9), where r_{xx} is the auto-correlation function of the input signal. The PSD and frequency were computed by Equations (10) and (11), where N_{sp} and Δt are the number of input data points and the sampling interval, respectively [34]:

$$p_{xx} = \sum_{m=-\infty}^{\infty} r_{xx}(m) e^{-j\omega m} \quad (9)$$

$$PSD_n = \frac{a^2 + b^2}{N_{sp}} \quad (10)$$

$$f_n = \frac{n}{N_{sp} \Delta t} \quad (11)$$

3. Results and Discussion

Figure 5a,b shows two types of OHP working conditions with different amounts of charge. Under constant heating ($Q = 20 \text{ W}$) and a certain range of charge (volume fraction (VF) = 14.7%), the OHP system temperature shows stable oscillatory behavior. However, if this range is exceeded, the working status will change from stable to intermittently unstable behavior. As shown in Figure 5a, the temperature oscillation of the evaporation section is constantly maintained in the range of 50–60 $^{\circ}\text{C}$. However, when VF increased to 24.5% with the same heat flux, the temperature of the evaporation section largely fluctuated from 60 to 70 $^{\circ}\text{C}$. When the Q was 10 W and the VF increased from 4.9% to 9.8%, the thermal resistance of OHP decreased from 1.5 to 1.43 K/W. However, when the VF increased to 14.7%, the thermal resistance of OHP increased to 1.66 K/W due to intermittent temperature fluctuations. When Q was 14 W, the minimum value of the thermal resistance (1.29 K/W) was observed at a VF of

14.7%. When Q increased to 20 W, the optimal value of VF was still 14.7% and the thermal resistance of OHP was 1.11 K/W. Generally, as VF increased, the thermal resistance of OHP decreased firstly, and then increased with increasing VF, as shown in Figure 5c. This is because if the charged amount of working fluid is insufficient, the working fluid cannot be sufficiently supplied to the evaporator section of OHP, resulting in a dry-out and increased OHP thermal resistance. If Q also increases, the dry-out phenomena in the evaporator becomes more serious and the thermal resistance of OHP increases, as shown in the Figure 5c with $VF = 4.9\%$. With the increase of VF, dry-out is well activated in the evaporation section of OHP and thermal resistance of OHP also reduces. However, when the amount of working fluid is not excessive, the pressure drop will increase between the liquid and pipe wall, the motion of working fluid will be resisted, intermittent fluctuated operation occurs, and then subsequently, the thermal resistance will increase. When VF is sufficiently large with an increasing Q , the temperature difference will also increase between the evaporator and condensation sections. This will lead to an increased pressure difference between working fluids in both sections. Heat transfer is stable and thermal resistance is reduced at a VF of 9.8–14.7%, as shown in Figure 5c. This means that the optimum charging rate of an OHP system should be correctly determined. Figure 5d shows a certain optimum and maximum criteria range for the charging rate, which is observed as a working condition.

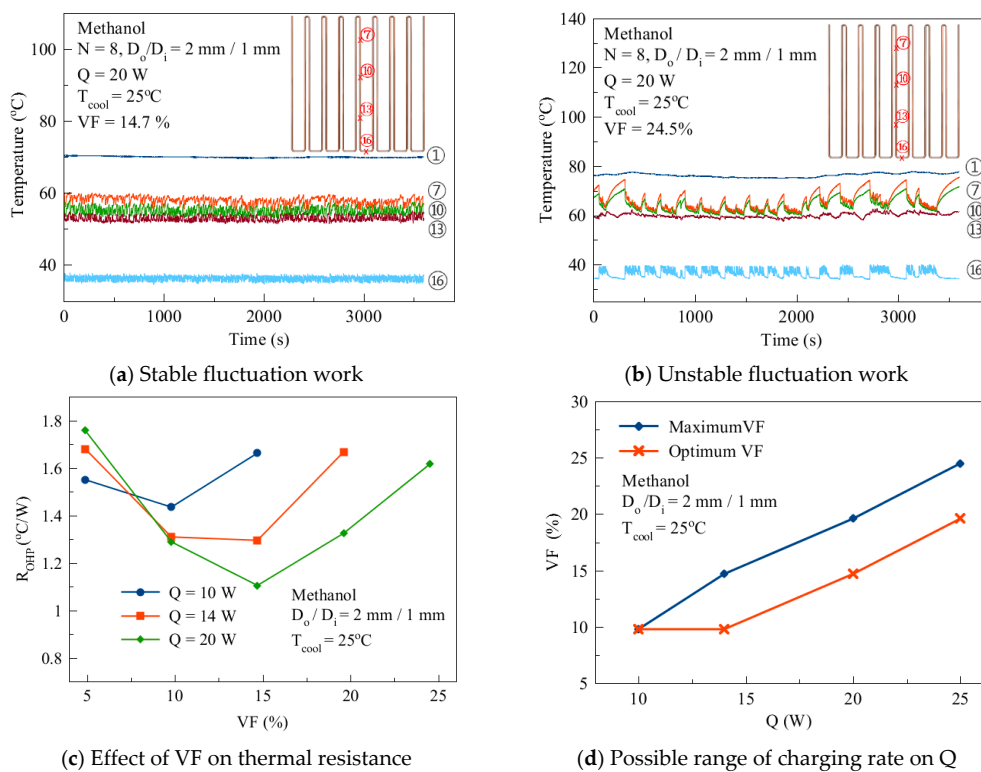


Figure 5. Effect of different charged volume fractions (VF).

The contact thermal resistance between the tube and the heater or cooling plate is affected by the diameter of the tube. Figure 6 shows the thermal resistance of the cooling system between the heater surface and the cooling plate under a constant heating rate in the OHP with different tube diameters and with different amounts of charge. When the D_o/D_i was 1.8 mm/0.8 mm, the optimal VF was about 15%. When the D_o/D_i was 2 mm/1 mm, the optimal VF was 10–15%. However, when the D_o/D_i was 2.4 mm/1.4 mm, the optimal VF was about 2–10%. From this, we know that the smaller the pipe diameter is, the bigger the optimal VF and the maximum VF are. This is because the larger the diameter, the larger the volume of OHP; pressure changes in the working fluid are also slow. However, in contrast, the smaller the diameter, the larger the pressure drop. Figure 6d also shows the effect of Q on thermal resistance with different VFs. The figure shows that the best working performance in terms

of the thermal resistance was obtained when VF was 9.8%. When VF was 9.8%, the plot line trend of thermal resistance with Q was not steeper than a VF of 14.7%. This means that the optimum charging rate is a VF of 9.8%.

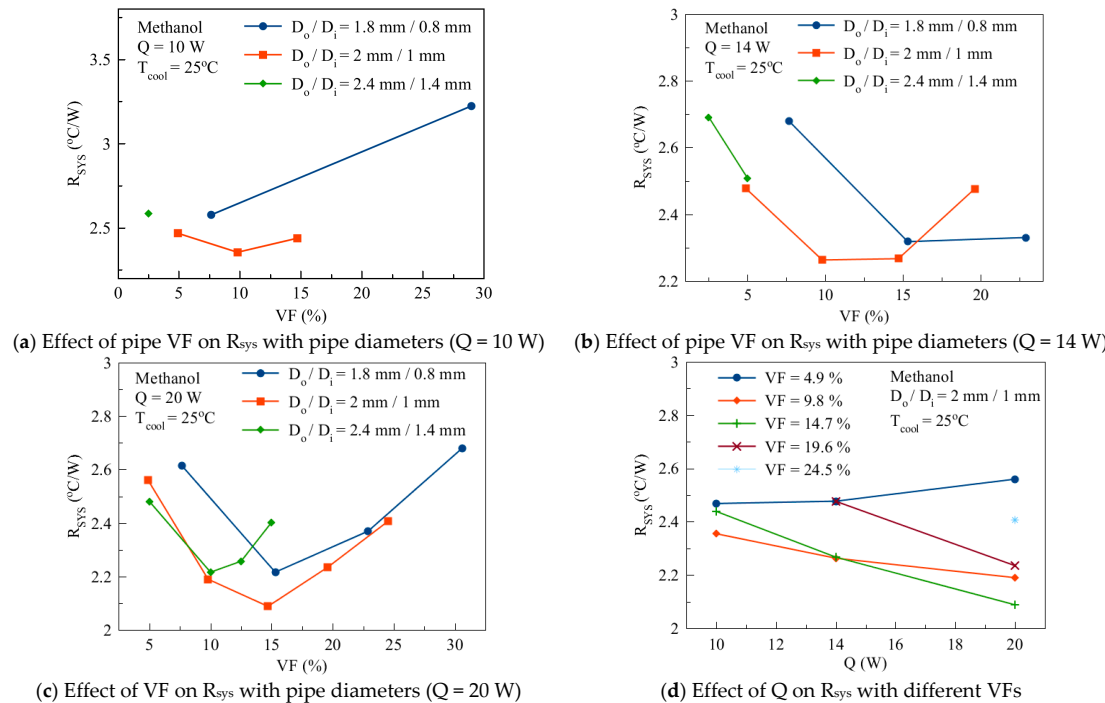


Figure 6. Effect of OHP pipe diameters on R_{sys} with different Q and VF.

Figure 7 shows the PSD of temperature position no. 13 with a D_o/D_i of 2 mm/1 mm and a VF of 9.8% with different heat fluxes. As shown in Figure 7a–d, when Q was 10 W, a larger PSD was distributed in the low frequency region (0–0.75 Hz). In the high frequency region, the PSD was small with a value of less than 1. When Q increased to 14 W between 0.075 and 0.125 Hz, PSD obviously increased. Compared with Q values of 10 and 14 W, PSD obviously increased across the full frequency range when Q was 20 W.

As shown in Figure 8a–d, with a T_{cool} of 20 °C, the peak appeared near to 0.75 Hz and was relatively wide. When the T_{cool} rose to 25 °C (Figure 8c), the peak was significantly narrower. When the T_{cool} continued to rise to 30 °C, not only did the peak disappear completely, PSD also decreased in the full frequency region. From this behavior, it can be understood that when the heating temperature increases or the coolant temperature decreases, the temperature difference will increase between the evaporation section and the condensation section. Thus, the pressure gradient also increases, the working fluid movement will be smooth, and larger PSD values will be distributed in the high frequency region.

Figure 9 shows the experimental result with an orientation change of D_o/D_i = 2 mm/1 mm under the experimental conditions of a VF of 9.8%, a Q of 14 W, and a T_{cool} of 25 °C. When the α -angle was 0°, the peak frequency appeared between 0.075 and 0.1 Hz. When the α -angle increased to 5°, the peak moved to the low frequency region. After the α -angle had increased to 10°, the peak almost disappeared, and in the low frequency region, the PSD increased significantly. Similarly, when β increased, the peak value of PSD between 0.05 and 0.1 Hz gradually reduced, and due to the increase in intermittent oscillation, the PSD in the low frequency region increased. We know from this that as the α -angle (or β -angle) increases, intermittent oscillations occur, and larger values of PSD migrate from the high frequency region to the low frequency region and the thermal resistance increases. This is because the increase of the α -angle causes the gravity component $g \sin(\alpha)$ to also decrease. However,

because the α -angle can increase the uneven distribution of the head, it has a better performance than the β -angle.

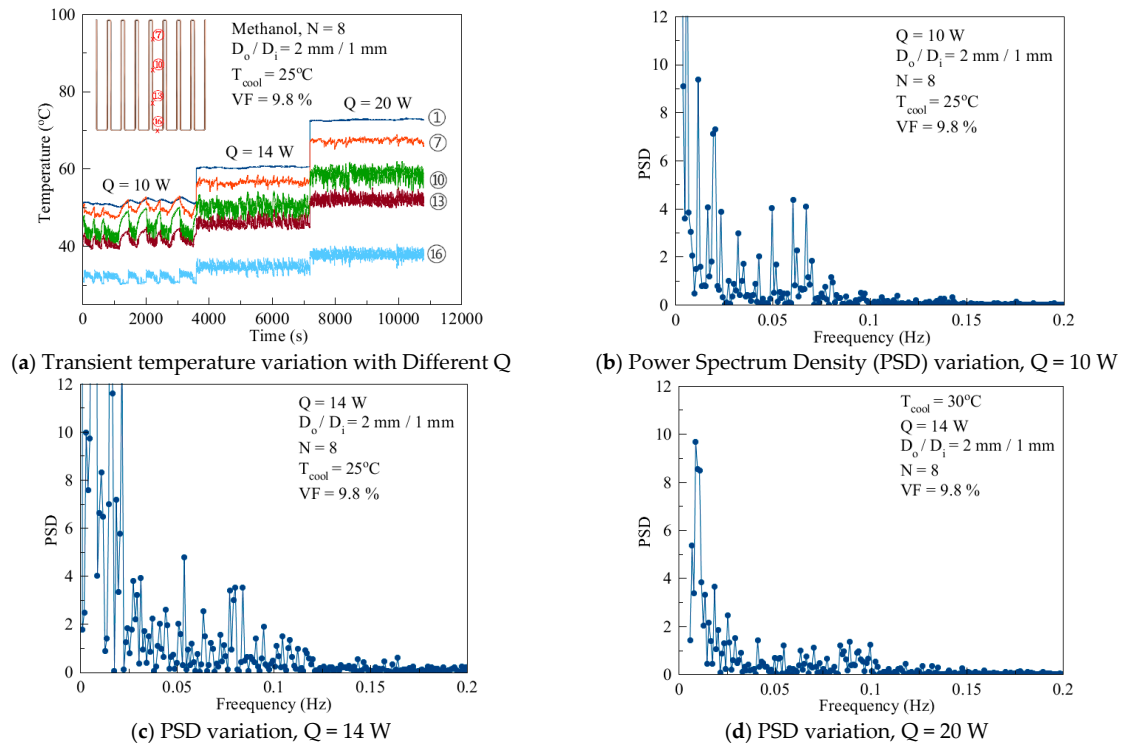


Figure 7. Seven PSD variation with different supplied heating rates.

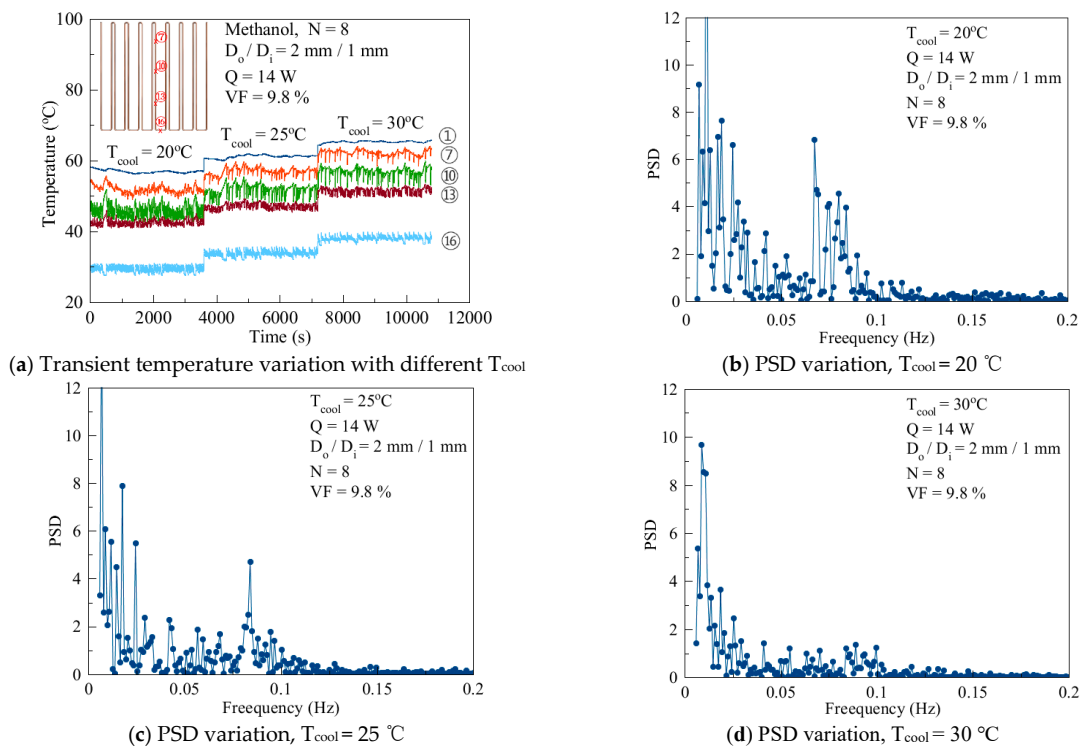


Figure 8. PSD variation with different coolant temperatures.

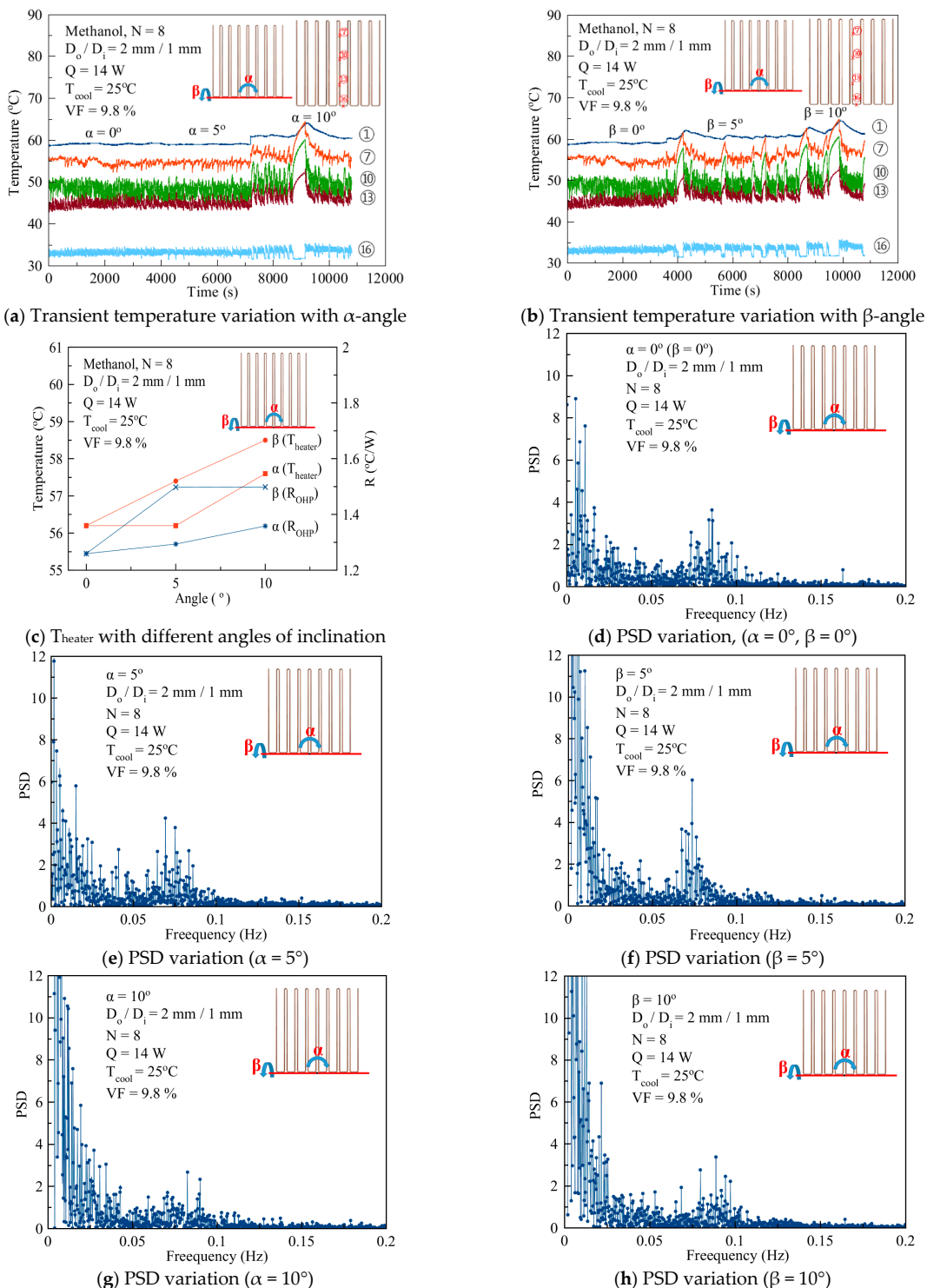


Figure 9. PSD variation with different inclination angles ($Q = 14 \text{ W}$, α - and β -angle).

4. Conclusions

In the present study, an OHP cooling system design for a Li-ion battery with a long evaporator section, a short condensing section, and eight turns, was proposed. The conclusions of experiments on various parameters and a PSD analysis are as follows:

- The heat transfer performance of the OHP system was found to be mainly dependent on the filling rate of the working fluid, that is, the greater the heating rate, the greater the optimal VF.

- Under the same heating and cooling conditions, the thermal performance and stability of the OHP system was optimal at D_o/D_i of 2 mm/1 mm.
- The OHP could be operated normally when the α -angle (or β) was in the range 1–5°. As the angle increased, the operation became unstable with large intermittent fluctuations.
- The average temperature of the heater was maintained at around 55 °C as a design goal with the following parameters: $D_o/D_i = 2$ mm/1 mm, $Q = 14$ W, $T_{cool} = 25$ °C, and $VF = 9.8\%$. This meets the basic requirements for battery cooling.

Author Contributions: R.-G.C. conducted the experiments and analysis; S.-H.R. supervised and analyzed the research results; this research was managed and supported by S.-H.R.

Funding: This research was funded by Basic Science Research Program through the National Research Foundation of Korea (NRF), Ministry of Education (Grant No. NRF-2016R1D1A1B03930495).

Acknowledgments: This research was supported by Basic Science Research Program through the National Research Foundation of Korea (NRF) funded by the Ministry of Education (No. NRF-2016R1D1A1B03930495).

Conflicts of Interest: The authors declare no conflict of interest.

Abbreviations

Bo	Bond Number
DC	Direct Current
OHP	Oscillating heat pipe
PSD	Power Spectrum Density (Energy/frequency)
PCM	Phase Change Material
VF	Volume fraction, ((Volume of charged working fluid)/(Total volume of OHP)) × 100%
Nomenclature	
A	Real part
B	Imaginary part
c_i	Coverage factor
D_{cr}	Critical diameter (m)
D_i	Inner diameter (m)
D_o	Outer diameter (m)
g	Gravitational acceleration (m/s ²)
I	Electric current (A)
n	Sampling number
N	Turn of number of OHP
N_{sp}	Number of input data points
\bar{T}_{heater}	Average temperature of heater (°C)
\bar{T}_{evap}	Average temperature of evaporator section of OHP (°C)
\bar{T}_{cond}	Average temperature of condenser section of OHP (°C)
T_{cool}	Temperature of coolant (°C)
R_{OHP}	Thermal resistance of OHP (W/°C)
R_{SYS}	Thermal resistance of system (W/°C)
r_{xx}	Auto-correlation function of the input signal
Q	Heating of heater (W)
u_c	Combined uncertainty
u_i	Standard uncertainty
v_i	Degree of freedom
v_{eff}	Effective degree of freedom
V	Voltage (W)
x_i	Parameters of the thermal resistance

Greek Letters

α	Angle (°)
β	Angle (°)
σ	Surface Tension (N/m)
ρ_l	Density of liquid (kg/m ³)
ρ_v	Density of vapor (kg/m ³)
σ_i	Standard error
Δt	Sampling interval (s)
ΔT	Temperature difference (°C)

References

- International Energy Agency. *Global EV Outlook 2018*; International Energy Agency: Paris, France, 2018; pp. 58–59.
- Thomas, B.R.; David, L. *Linden's Handbook of Batteries*, 4rd ed.; McGraw-Hill: New York, NY, USA, 2011; pp. 331–417.
- Li, H.L.; Su, J.R. Cycle-life prediction model studies of lithium-ion batteries. *Chin. J. Power Sources* **2008**, *32*, 242–246.
- Forgez, C.; Do, D.V.; Friedrich, G. Thermal modeling of a cylindrical LiFePO₄/graphite lithium-ion battery. *J. Power Sources* **2010**, *195*, 2961–2968. [[CrossRef](#)]
- Jeon, D.H.; Baek, S.M. Thermal modeling of cylindrical lithium ion battery during discharge cycle. *Energy Convers. Manag.* **2011**, *52*, 2973–2981. [[CrossRef](#)]
- Viswanathan, V.V.; Choi, D.; Wang, D. Effect of entropy change of lithium intercalation in cathodes and anodes on Li-ion battery thermal management. *J. Power Sources* **2010**, *195*, 3720–3729. [[CrossRef](#)]
- Xia, G.D.; Cao, L.; Bi, G.L. A review on battery thermal management in electric vehicle application. *J. Power Sources* **2017**, *367*, 90–105. [[CrossRef](#)]
- Heubner, C.; Schneider, M.; LaMmel, C. Local Heat Generation in a Single Stack Lithium Ion Battery Cell. *Electrochim. Acta* **2015**, *186*, 404–412. [[CrossRef](#)]
- Liu, G.M.; Ouyang, M.; Lu, L.G. Analysis of the heat generation of lithium-ion battery during charging and discharging considering different influencing factors. *J. Therm. Anal. Calorim.* **2014**, *116*, 1001–1010. [[CrossRef](#)]
- Bandhauer, T.M.; Garimella, S.; Fuller, T.F. Temperature-dependent electrochemical heat generation in a commercial lithium-ion battery. *J. Power Sources* **2014**, *247*, 618–628. [[CrossRef](#)]
- Panchal, S.; Dincer, I.; Agelin-Chaab, M.; Fraser, R.; Fowler, M. Experimental and theoretical investigations of heat generation rates for a water cooled LiFePO₄ battery. *Int. J. Heat Mass Transf.* **2016**, *101*, 1093–1102. [[CrossRef](#)]
- Choi, Y.S.; Kang, D.M. Prediction of thermal behaviors of an air-cooled lithium-ion battery system for hybrid electric vehicles. *J. Power Sources* **2014**, *270*, 273–280. [[CrossRef](#)]
- Yu, K.Y.; Yang, X.; Cheng, Y.Z. Thermal analysis and two-directional air flow thermal management for lithium-ion battery pack. *J. Power Sources* **2014**, *270*, 193–200. [[CrossRef](#)]
- Ling, Z.Y.; Wang, F.X.; Fang, X.M. Hybrid thermal management system for lithium ion batteries combining phase change materials with forced-air cooling. *Appl. Energy* **2015**, *148*, 403–409. [[CrossRef](#)]
- Bai, F.F.; Chen, M.B.; Song, W.J.; Feng, Z.P. Thermal management performances of PCM/water cooling-plate using for lithium-ion battery module based on non-uniform internal heat source. *Appl. Therm. Eng.* **2017**, *126*, 17–27. [[CrossRef](#)]
- Tong, W.; Somasundaram, K.; Birgersson, E. Numerical investigation of water cooling for a lithium-ion bipolar battery pack. *Int. J. Therm. Sci.* **2015**, *94*, 259–269. [[CrossRef](#)]
- Huo, Y.T.; Rao, Z.H.; Liu, X.J. Investigation of power battery thermal management by using mini-channel cold plate. *Energy Convers. Manag.* **2015**, *89*, 387–395. [[CrossRef](#)]
- Panchal, S.; Haji, M.; Akhoundzadeh, K.; Raahemifar, M.; Fraser, R.; Fowler, M. Heat and mass transfer modeling and investigation of multiple LiFePO₄/graphite batteries in a pack at low C-rates with water-cooling. *Int. J. Heat Mass Transf.* **2019**, *135*, 368–377. [[CrossRef](#)]

19. Liu, F.F.; Lan, F.C.; Chen, J.Q. Dynamic thermal characteristics of heat pipe via segmented thermal resistance model for electric vehicle battery cooling. *J. Power Sources* **2016**, *321*, 57–70. [[CrossRef](#)]
20. Wang, Q.; Jiang, B.; Xue, Q.F.; Sun, H.L.; Li, B.; Zou, H.M.; Yan, Y.Y. Experimental investigation on EV battery cooling and heating by heat pipes. *Appl. Therm. Eng.* **2015**, *88*, 54–60. [[CrossRef](#)]
21. Hong, S.H.; Wang, S.F.; Zhang, Z.G. Multiple orientations research on heat transfer performances of Ultra-Thin Loop Heat Pipes with different evaporator structures. *Int. J. Heat Mass Transf.* **2016**, *98*, 415–425. [[CrossRef](#)]
22. Rao, Z.H.; Huo, Y.T.; Liu, X.J. Experimental study of an OHP-cooled thermal management system for electric vehicle power battery. *Exp. Therm. Fluid Sci.* **2014**, *57*, 20–26. [[CrossRef](#)]
23. Wang, Q.C.; Rao, Z.H.; Huo, Y.T.; Wang, S.F. Thermal performance of phase change material/oscillating heat pipe-based battery thermal management system. *Int. J. Therm. Sci.* **2016**, *102*, 9–16. [[CrossRef](#)]
24. Qu, J.; Wang, C.; LI, X.J.; Wang, H. Heat transfer performance of flexible oscillating heat pipes for electric/hybrid-electric vehicle battery thermal management. *Appl. Therm. Eng.* **2018**, *135*, 1–9. [[CrossRef](#)]
25. Chi, R.G.; Chung, W.S.; Rhi, S.H. Thermal Characteristics of an Oscillating Heat Pipe Cooling System for Electric Vehicle Li-Ion Batteries. *Energies* **2018**, *11*, 655.
26. Zhao, R.; Zhang, S.; Liu, J. A review of thermal performance improving methods of lithium ion battery: Electrode modification and thermal management system. *J. Power Sources* **2015**, *299*, 557–577. [[CrossRef](#)]
27. Liu, H.Q.; Wei, Z.B.; He, W.D.; Zhao, J.Y. Thermal issues about Li-ion batteries and recent progress in battery thermal management systems: A review. *Energy Convers. Manag.* **2017**, *150*, 304–330. [[CrossRef](#)]
28. Chen, D.F.; Jiang, J.C.; Kim, G.H.; Yang, C.B.; Pesaran, A. Comparison of different cooling methods for lithium ion battery cells. *Appl. Therm. Eng.* **2016**, *97*, 846–854. [[CrossRef](#)]
29. Hu, Q.W.; Li, W.B.; Wang, Z.C. Review on Cooling Technique for Li-ion Battery Pack. *Mar. Electr. Electron. Eng.* **2016**, *36*, 53–58.
30. Riffat, S.; Mempouo, B.; Fang, W. Phase change material developments: A review. *Int. J. Ambient. Energy* **2013**, *36*, 102–115. [[CrossRef](#)]
31. Lin, Y.H.; Kang, S.W.; Chen, H.L. Effect of silver nano-fluid on pulsating heat pipe thermal performance. *Appl. Therm. Eng.* **2008**, *28*, 1312–1317. [[CrossRef](#)]
32. Cao, X.L.; Wang, W.; Chen, J.; Li, X.L.; Yu, S.X. Experimental Investigation on the Start-Up Characteristic of a Pulsating Heat Pipe. *Fluid Mach.* **2009**, *37*, 57–60.
33. Liang, J.W.; Chen, L.C.; He, G. *Error Theory and Data Processing*, 2nd ed.; China Metrology Publishing House: Beijing, China, 2001; pp. 67–71.
34. Origin Lab Corp. Help Manual. 2019. Available online: <https://www.originlab.com/doc/Origin-Help/FFT1-Algorithm> (accessed on 20 January 2019).



© 2019 by the authors. Licensee MDPI, Basel, Switzerland. This article is an open access article distributed under the terms and conditions of the Creative Commons Attribution (CC BY) license (<http://creativecommons.org/licenses/by/4.0/>).